

The optimization of evaporation rate in graphene-water system by machine learning algorithm

Cite as: J. Appl. Phys. 135, 135302 (2024); doi: 10.1063/5.0187236

Submitted: 12 November 2023 · Accepted: 17 March 2024 ·

Published Online: 3 April 2024



Degao Qiao,^{1,2} Ming Yang,^{1,a)} Yin Gao,¹ Jue Hou,² Xingli Zhang,^{2,b)} and Hang Zhang^{1,c)}

AFFILIATIONS

¹Institute of Engineering Thermophysics, Chinese Academy of Sciences, Beijing 100190, China

²College of Mechanical and Electrical Engineering, Northeast Forestry University, Harbin 150040, China

Note: This paper is part of the special topic, Machine Learning for Thermal Transport.

^{a)}Author to whom correspondence should be addressed: yangming@iet.cn

^{b)}zhang-xingli@nefu.edu.cn

^{c)}zhanghang@iet.cn

ABSTRACT

Solar interfacial evaporation, as a novel practical freshwater production method, requires continuous research on how to improve the evaporation rates to increase water production. In this study, sets of data were obtained from molecule dynamics simulation and literature, in which the parameters included height, diameter, height–radius ratio, evaporation efficiency, and evaporation rate. Initially, the correlation between the four input parameters and the output of the evaporation rate was examined through traditional pairwise plots and Pearson correlation analysis, revealing weak correlations. Subsequently, the accuracy and generalization performance of the evaporation rate prediction models established by neural network and random forest were compared, with the latter demonstrating superior performance and reliability confirmed via random data extraction. Furthermore, the impact of different percentages (10%, 20%, and 30%) of the data on the model performance was explored, and the result indicated that the model performance is better when the test set is 20% and all the constructed model converge. Moreover, the mean absolute error and mean squared error of the evaporation rate prediction model for the three ratios were calculated to evaluate their performance. However, the relationship between the height–radius ratio and optimal evaporation rate was investigated using the enumeration method, and it was determined that the evaporation efficiency was optimal when the height–radius ratio was 6. Finally, the importance of height, diameter, height–radius ratio, and evaporation efficiency were calculated to optimize evaporator structure, increase evaporation rate, and facilitate the application of interfacial evaporation in solar desalination.

© 2024 Author(s). All article content, except where otherwise noted, is licensed under a Creative Commons Attribution (CC BY) license (<https://creativecommons.org/licenses/by/4.0/>). <https://doi.org/10.1063/5.0187236>

I. INTRODUCTION

Clean water production is important for human well-being and sustainable development. However, conventional water treatment technologies have the disadvantage of significant energy consumption and greenhouse gas emissions.^{1–4} Solar energy is a clean energy source that is constantly replenished by nature and its utilization is not geographically limited. Therefore, the use of solar energy to promote water evaporation provides a feasible solution for water treatment to reduce energy consumption and save costs. However, the energy transfer efficiency during solar evaporation

under natural conditions is less than 20%, which is mainly due to the high heat loss during evaporation.⁵ Therefore, interfacial evaporation systems have attracted increasing attention from relevant researchers. To increase water production rate, researchers have been investigating ways to increase the evaporation rate. It has been found that optimizing the size and shape of the solar evaporator is crucial for improving heat and mass transfer coupling during the interfacial evaporation process, which can substantially increase the evaporation rate.⁶ In order to quantitatively understand the coupled multiple physical fields involved in the solar-driven

06 April 2024 06:03:38

interfacial evaporation device, Meng and colleagues employed a unified experimental and numerical method. Specifically, they first quantified the interaction between optical and transport processes in the solar interface evaporator to guide the rational design of materials and structures. Then, they determined the optimal location and thickness of the evaporation interface. Finally, they verified the modeling framework through special experiments and designed a high-performance solar evaporator with optimized interface performance, which achieved a final evaporation rate of $5.38 \text{ kg m}^{-2} \text{ h}^{-1}$, representing a 12% increase compared with the evaporation rate at the interface region under one solar condition.⁷ Similarly, Lim *et al.* fabricated PAP hydrogels into three-dimensional structures to maximize the total area of the water–air interface and increase the evaporation rate. By varying the aspect ratio, they investigated the impact of 3D geometry on the evaporation rate and found that the higher length-to-diameter ratio of the hydrogel, the higher the evaporation rate. The evaporation rate under solar irradiation was observed to reach its maximum value ($4.145 \text{ kg m}^{-2} \text{ h}^{-1}$) at this optimized aspect ratio. This study also highlighted that the influence of size and shape on the evaporation rate could not be ignored. Furthermore, it was revealed that the height of the heat insulation layer has a significant impact on the evaporation rate, primarily through its dynamic factor affecting water production rate of interface evaporation. The diameter of evaporator plays a crucial role in determining the area of the evaporator, which directly affects the strength of the heat radiation, heat conduction, and heat convection pairs. In addition, the area is closely related to the thermal insulation performance of the evaporator. Therefore, optimizing the height–radius ratio could help achieve a balance between heat and mass transfer, ultimately leading to an increase of evaporation rate.

Optimizing the height-to-radius ratio of the evaporator involves the rational design of structural parameters, which could be accomplished through machine learning to optimize multiple input variables. Yang *et al.* combined machine learning algorithms with molecular dynamics to predict the properties of glass, mitigating deficiencies inherent in single-method approaches. Through analyzing molecular dynamics-generated data sets and subsequent comparing model performance following hyperparameter tuning, machine learning models and associated hyperparameters suitable for predicting glass properties were identified. The resulting model could be used to rapidly and inexpensively screen multi-component glass constituents, resulting in a database of component properties that could predict the properties of various combinations of components.⁸ Joshi *et al.* investigated the stress–strain relationships of fixed aspect ratio silver nanowires at different temperatures and then used machine learning to establish a model to predict the ultimate tensile strength based on this relationship. R^2 values demonstrated that nearly 86%–94% of forecasted data falls within the regression line.⁹ Yang further developed an accurate and convenient method to predict the hourly output of tubular solar stills through the machine learning. The effectiveness of different machine learning algorithms, including classical artificial neural networks, random forest, and traditional multiple linear regression models, were compared, with random forests being determined to exhibit lower sensitivity to hyperparameters, high precision, and robustness, making them well-suited for yield prediction in the

context of tubular solar stills.¹⁰ In summary, the application of machine learning is clearly expected to simulate interactions between multiple input variables, thereby optimizing evaporator size and structure.

In the past research on interfacial evaporation mainly focuses on enhancing the evaporation rate by changing the material properties and lacks the study of the geometry, so we have performed the geometric parameter of height-to-radius ratio of the interfacial evaporator by machine learning algorithms. In this study, 200 sets of data were constructed through molecule dynamics simulation and literature review. Initially, the relationship between the input parameters and the output evaporation rate was examined through traditional pairwise plots and Pearson correlation analysis. Next, neural network and random forest models were developed to predict the evaporation rate, and the latter was found to have greater accuracy and generalization ability compared to the former. Then, the reliability of the model was validated through random sampling, and the impact of different proportions of the test set data on model performance was explored. Mean absolute error (MAE) and mean squared error (MSE) were computed to benchmark the performance of the evaporation rate prediction at each rate. In addition, the relationship between the height–radius ratio and maximum attainable evaporation rate was established by an enumeration method. The characteristic importance of the height, diameter, height–radius ratio, and evaporation efficiency was also determined. Finally, the optimal height-to-radius ratio of the insulating water transport layer of the interfacial evaporator was obtained from the data collected from the literature and simulations while using a machine learning algorithm. Application of the optimized evaporator structure could increase the evaporate rate, thereby promoting its potential use in solar desalination.

II. MODEL AND METHOD

A. Molecular dynamics method

Non-equilibrium molecular dynamics (NEMD) simulations are performed using LAMMPS (Large-scale Atomic/Molecular Massively Parallel Simulator) molecular dynamics simulator with setting time step as 1 fs throughout. The adaptive intermolecular reactive empirical bond order (AIREBO) potential is used to describe the interactions of the carbon atoms within same layers, and the Lennard–Jones potential is used to describe the Vander Waals interactions for C–C atoms between different layers. As shown in Fig. 1, the sodium chloride solution with the density of 1.5 mol/l was uniformly mixed under graphene layers, which acted as a heat insulation and the water absorption layer. The porous structure is formed by periodically removing carbon atoms from the upper layer of graphene. The simulation system consisted of 680 water molecules and 2560 carbon atoms, and the free boundary conditions were employed in all directions. Prior to the evaporation simulation, the system was equilibrated in the NPT ensemble at 1 atm and 298 K for 10 ns to ensure proper mixing and to obtain the real density. Then, an evaporation simulation was performed in the NVT ensemble at 393 K for 1000 ns. Last, the Ewald method was utilized to compute the remote interactions. To ensure the reliability of the simulation results, each simulation was repeated three times with different initial velocities.

06 April 2024 06:03:38

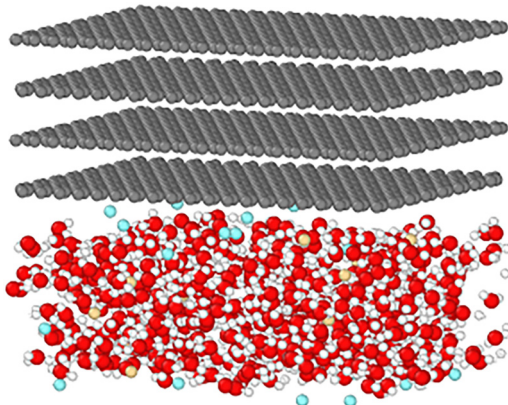


FIG. 1. Simulation system of interfacial evaporation.

B. Random forest

Random forest is a typical integration method that combines multiple decision trees into a single model to improve performance. It is widely used in lots of scientific and engineering fields, such as statistics, materials science, and biology. The main steps in constructing a random forest are as follows.

1. Data preprocessing

First, for the obtained data set P , n sets of data were produced as a subset of N -tree through bootstrap resampling method, and then divided into training sets and test sets according to a certain proportion. Before the training, all feature data were normalized into standard data with a mean of 0 and a standard deviation of 1.

2. Model establishment

After data preprocessing, n decision trees were generated according to the randomized algorithm, and each generated decision tree was different from other decision trees to ensure diversity. The output of the random forest was the weighted average of n decision trees, thus achieving the purpose of reducing variance and improving accuracy.

3. Model evaluation

The partitioned test set was not used for model training, so it can be used to verify the accuracy of the model. If the accuracy of the test set is much lower than that of the training set, the model is considered overfitting. If the accuracy of both the test set and the training set is low, the model is considered underfitting and need to be retrained. If the accuracy of both the test set and the training set are high and close, the model is considered to have a good training effect.

C. Neural network

- (1) First, the data set is divided into a training set and a test set, then the weight in the neural network is initialized to a smaller

value and propagated through the network layer by layer, and finally, the predicted value of evaporation rate is obtained. For each sample (X_k, Y_k) in the data set, the error E_k can be calculated as follows:

$$E_k = \frac{1}{2} (y_0 - y_k)^2. \quad (1.1)$$

- (2) Set the weight between the output layer and the hidden layer as W_{ij} , the weight between the input layer and the hidden layer as V_{xj} , where i and j are the serial number of neurons in the hidden layer, and according to the backpropagation algorithm, error signals will be transmitted back through the network and W_{ij} and V_{xj} can be adjusted according to the following formula:

$$w_{ij_new} = -\theta \frac{\partial E_k}{\partial w_{ij}} + w_{ij}, \quad (1.2)$$

$$v_{xj_new} = -\theta \frac{\partial E_k}{\partial b_j} \cdot \frac{\partial b_j}{\partial \alpha_j} + v_{xj}, \quad (1.3)$$

where b_j is the output of the j th neuron of the hidden layer, α_j is the input of the j th neuron of the hidden layer, and $\theta \in (0 - 1)$ is the learning rate of the neural network. The larger the value of the learning rate, the faster the convergence rate.

- (3) Repeat (1) and (2) until the cut-off condition is reached.

D. Main flow chart and data sets

The primary research method is visually presented in Fig. 2. In the first stage, molecular dynamics simulation and previous literature extraction are employed to obtain necessary data. Subsequently, the predictive model for evaporation rate is developed using neural network and random forest algorithms as well as training and testing steps. Ultimately, a mapping relationship between the evaporator height, diameter, ratio of height to radius, evaporation efficiency, and evaporation rate is established, culminating in the formation of the aforementioned prediction model. Evaporation efficiency indicates the proportion of heat input that is converted to actual interfacial evaporated heat. Evaporation rate is the amount of water molecules evaporated per unit of time per unit of area. For the collected and calculated data set,^{11–68} $M = \{X, y\}_{1:t}$, with y representing the target variable, namely, evaporation rate, and X indicating the input descriptors encompassing evaporator height, diameter, the ratio of height to radius, and evaporation efficiency. As some data are missing, mean completion is utilized as a method of imputation. Table I provides a detailed distribution of the completed data set.

III. RESULTS AND DISCUSSION

A. Traditional data process

To determine the relationship between descriptors, two conventional data processing techniques were utilized for correlation analysis. As illustrated in Fig. 3, the pairwise plot provided the data

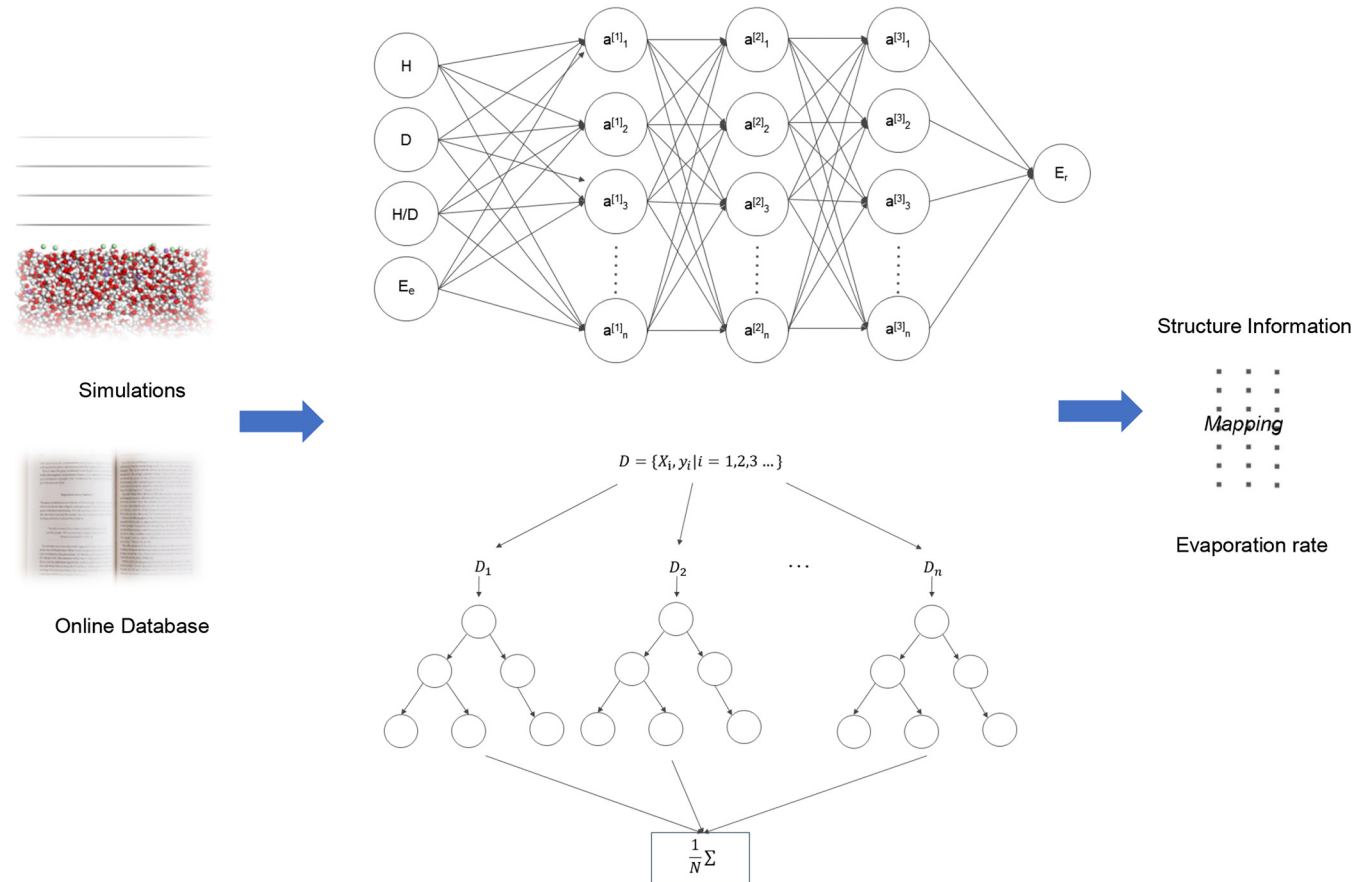


FIG. 2. Flow chart of machine learning training process.

distribution corresponding to each descriptor along the diagonal line, indicating a correlation between evaporation rate and height, diameter, and height-to-radius ratio of the heat insulating water-absorbing layer, while the evaporation efficiency showed no significant correlation due to its high concentration values in the collected data set. Conversely, the pair wise plot (PWP) approach was based on purely mathematical mappings within the data set and therefore did not weigh the importance of descriptors. To quantify the relationship between descriptors, Pearson correlation analysis

(PCA) was carried out, as depicted in Fig. 4. The strength of correlation between two descriptors becomes stronger when their respective coefficient value approaches 1 or -1 (a positive or negative correlation is indicated by regularity or irregularity in the value). The last row and column of Fig. 4 showed limited correlations between the insulation absorbent layer's height, diameter, height-to-radius ratio, and evaporation rate. However, as suggested in Fig. 3, all descriptor absolute values were low, indicating poor correlation with evaporation rate overall. Like the pair wise plot, Pearson correlation analysis could not produce satisfactory results regarding the relationship between descriptors and their importance.

TABLE I. The details of data set.

Descriptors	value	Number of samples
H	3.81×10^{-7} –20 cm	171
D	2.95×10^{-8} –16 cm	158
H/R	0.01–16	162
Evaporation efficiency	29%–220.34%	124
Evaporation rate	0.44–5.80 kg/m ² /h	200

B. Comparison of different machine learning algorithms

To identify a proficient machine learning model for predicting evaporation rates, extensive research involving multi-variable input and univariate output prediction was conducted. Neural networks and random forest models were found to be suitable for further investigation. After comparison, both models were employed to

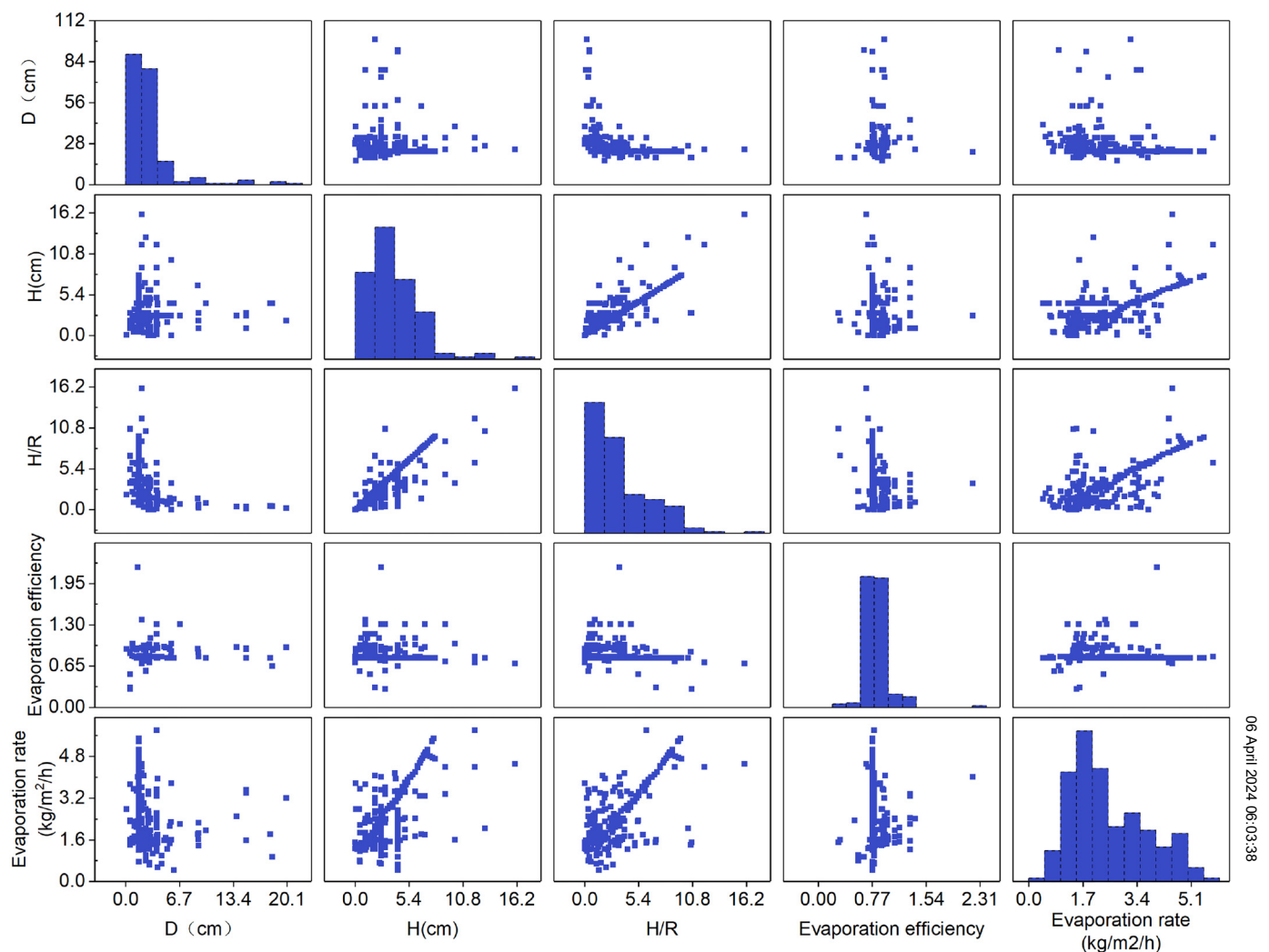


FIG. 3. Pair wise plots of data set.

forecast the evaporation rate, with the random forest outperforming the neural network due to its superior R^2 value closer to 1, which may be attributed to differences arising from model parameter adjustment in the training process, as illustrated in Figs. 5(a) and 5(b). During the training of two models, 80% of the acquired information was used as the training set while the rest formed the test set to enhance precision through applying the fivefold cross-validation technique. Compared with random forests, neural networks provide greater flexibility and parameters, availing more customization functions; however, this benefit comes with the disadvantage of prospectively challenging parameter configuration. Hence, random forest appears more appropriate for modeling evaporation rate prediction, particularly in cases involving multi-variable input and univariate output.

Furthermore, to assess the prediction accuracy of the evaporation rate model developed using the random forest algorithm, a random sampling of data points are utilized to compare actual values with predicted values. As depicted in Fig. 6, despite few apparent outliers, most of the predicted values for the randomly sampled data corresponded well with their actual values. Nevertheless, it is evident that poor performing predictions mainly arise at extreme values. Hence, by removing or substituting such anomalies from the data set, the accuracy of random forest predictions could be significantly enhanced.³ A synthesis of results obtained from Figs. 5(b) and 6 signifies that the resultant evaporation rate prediction model, derived from the random forest algorithm, demonstrates high precision and robust prediction capability.

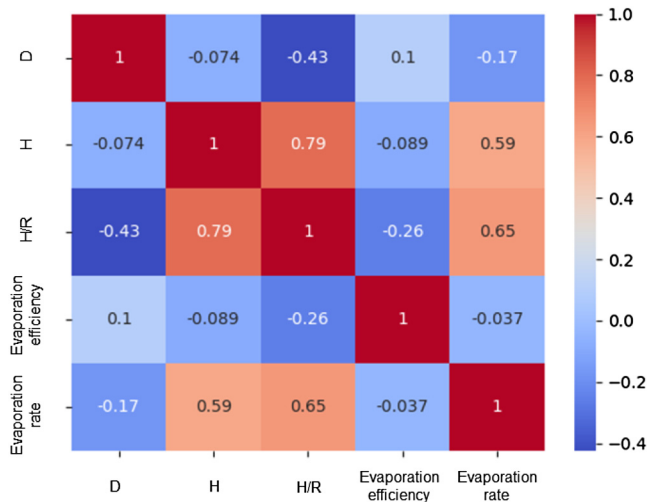


FIG. 4. Pearson correlation analysis of data set.

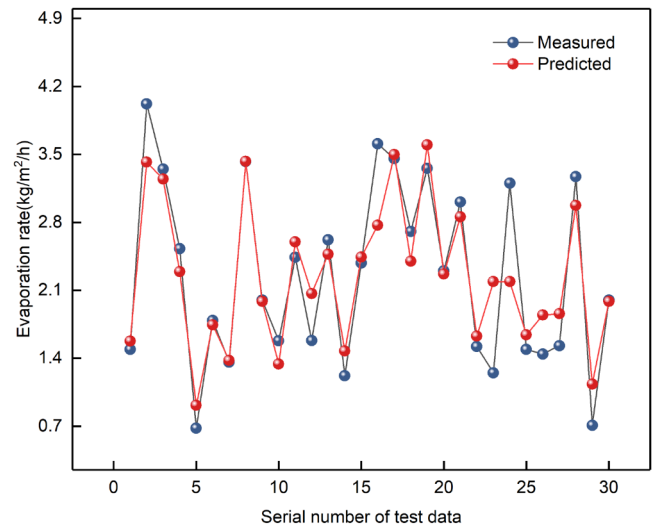


FIG. 6. Graph comparing actual and predicted values of random sampling.

C. Influence of the ratio of test set and training set

Taking into account the limited extent of data available, it is noteworthy that the size and composition of the training data set could significantly impact the quality of evaporation rate prediction models. Accordingly, an investigation was carried out to determine how dissimilar proportions of the training set and test set affect predictive performance. As elucidated in Figs. 7(a)–7(c), a series of models were trained using various test sets consisting of 10%, 20% and 30% employing the random forest algorithm. It could be observed that the model performance is better when the test set is

20% and a sufficiently reliable model could be acquired by using the current data volume.

Furthermore, in order to facilitate a comprehensive assessment of the predictive model efficacy, performance metrics such as the mean absolute error (MAE) and mean square error (MSE) were computed for different variations of training-test sets. As illustrated in Fig. 8, the results of MAE for the three models stand at 0.067 81, 0.062 31, and 0.061 22, whereas their MSEs, respectively, are 0.013 16, 0.012 11, and 0.013 29. These metrics indicate that the prediction models exhibit low MAE and MSE values, accentuating their robustness and similarity with other prediction models. This

06 April 2024 06:03:38

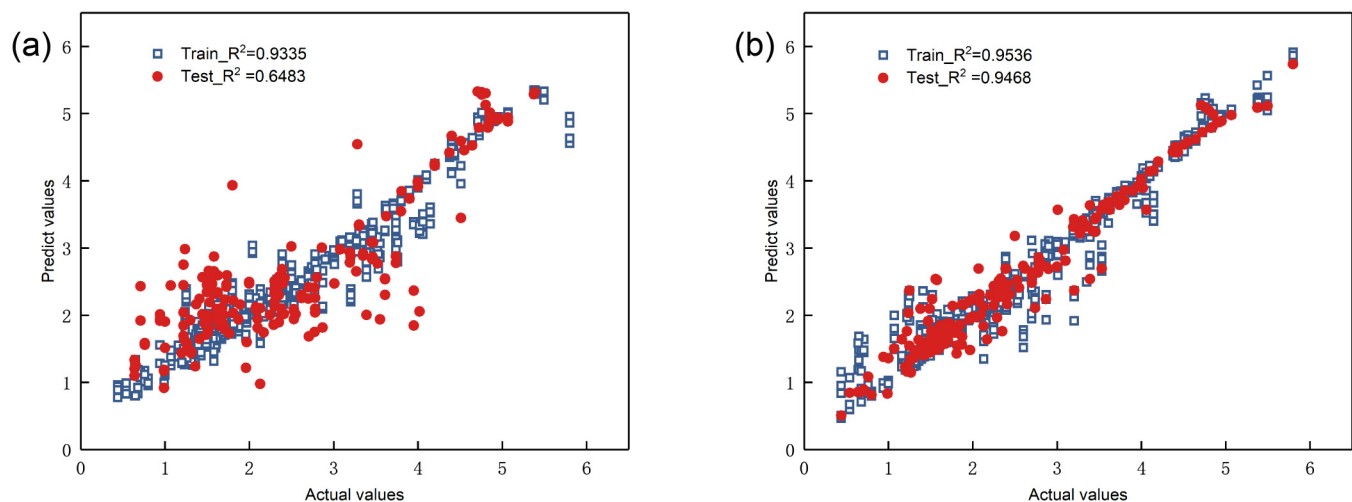


FIG. 5. Neural network training results (a) and random forest training results (b).

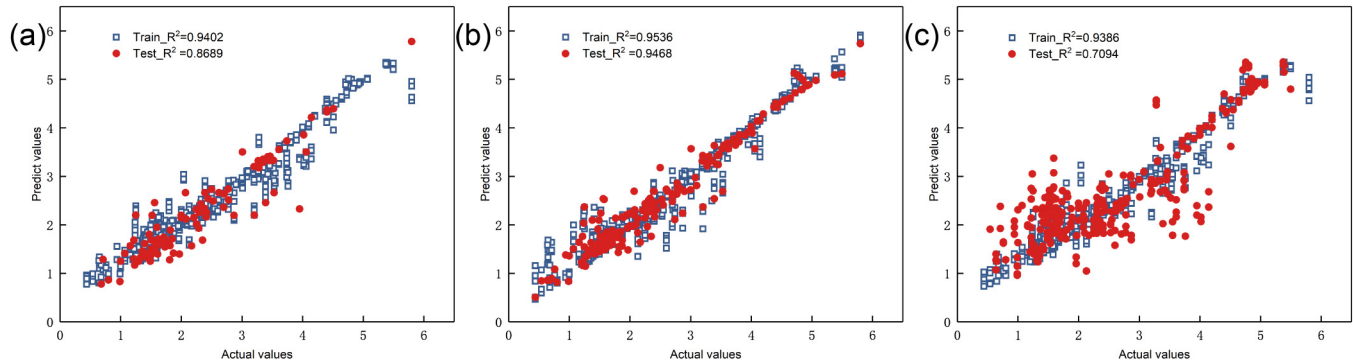


FIG. 7. Training results of different test set ratios: 10% (a), 20% (b), and 30% (c).

consistency corroborates the practicability of the proposed performance indices and bolsters confidence in the generality of the prediction model. Accordingly, the evaporation rate prediction model trained by employing the random forest algorithm boasts high accuracy and strong generalization capabilities, thereby minimizing the likelihood of overfitting events.

D. Random forest algorithm used to predict H/R

The utilization of the aforementioned machine learning algorithm facilitated the development of an evaporation rate prediction model. To identify the optimal height-to-radius ratio associated with the evaporator structure exhibiting the highest evaporation rate, the enumeration method was employed to produce multiple input variables for the prediction model. Afterward, diverse evaporation rate values were obtained by inputting these variables into the model for selection, thereby determining the maximum

evaporation rate and its height-to-radius ratio. Specifically, 2000 data sets representing input variables were generated via the enumeration method and fed into the trained model to predict the evaporation rate. Consequently, 2000 evaporation rate values were obtained from which the largest value was selected. Then, the ratio of height to radius represented a balance between heat and mass transfer behind both insulation and water transfer processes. As illustrated in Fig. 9, the scatterplot of the height-to-radius ratio and evaporation rate was plotted, which manifested that the height-to-radius ratio linked to the utmost evaporation rate was proximate to 6. This observation suggests that the thermal insulation absorbent layer height effect on water transfer rate and the diameter superimposition's thermal insulation impact can comprehend the maximal evaporation rate when their ratio stands at 6

06 April 2024 06:03:38

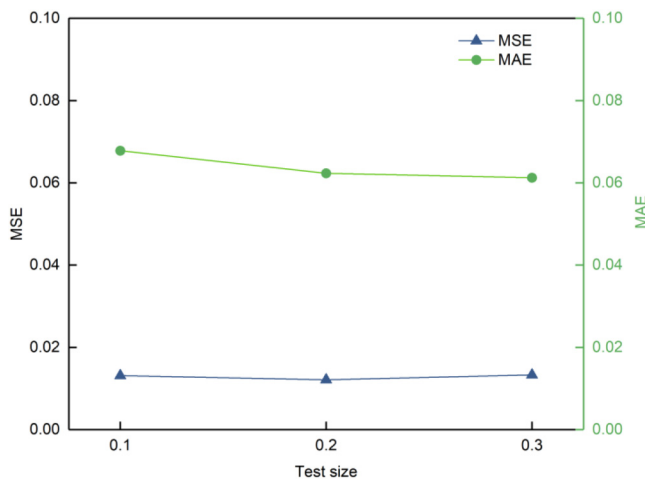


FIG. 8. Mean absolute error (MAE) and mean square error (MSE) of different test sets.

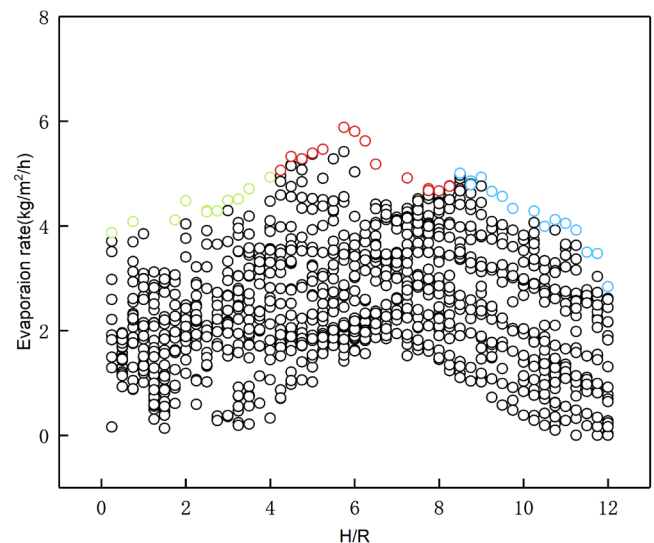


FIG. 9. The predicted result of height-to-radius coordinate.

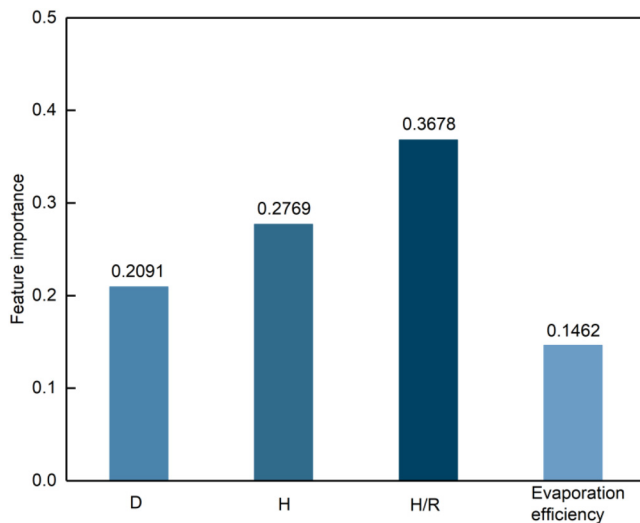


FIG. 10. The weight graph of input variables.

which is consistent with previous experimental results in other literature.¹⁰

Furthermore, a feature importance analysis using Random Forest (RF) was conducted to investigate the role of each parameter in the model calculation process. As depicted in Fig. 10, the feature importance rankings were as follows: diameter (20.91%), height (27.69%), ratio of height to radius (36.78%), and evaporation efficiency (14.62%). These rankings corresponded to the degree of contribution to the evaporation rate in each parameter. The height of the evaporator mainly affects the evaporation rate through dynamic factors that affect the water transfer rate from the supply of water for interface evaporation. On the other hand, the diameter of evaporator determines its area, which directly impacts heat radiation, conduction, and convection, and consequently its thermal insulation performance. The feature importance of the diameter is weaker than that of the height. It should be noted that higher heights could provide better insulation but slower water transfer rates, while larger diameters produce worse insulation but larger water transfer. Therefore, the ratio of height to radius represents a balance between heat and mass transfer behind both insulation and water transfer processes, hence its importance is greater. Furthermore, based on the collected data, researchers usually employ materials with optimal photothermal conversion efficiency, thereby achieving high evaporation efficiency and lessening its importance in the feature analysis.

IV. CONCLUSIONS

This study obtained a data set of 200 data entries on height, diameter, height-to-radius ratio, evaporation efficiency, and evaporation rate using molecule dynamics simulation and literature review. First of all, traditional pair wise plots and Pearson correlation analysis were employed to investigate the relationship between the four input parameters (height, diameter, height-to-radius ratio,

and evaporation efficiency) and the output parameter (evaporation rate), and a weak correlation was found among them. Subsequently, the prediction accuracy of two models for evaporation rate, neural network, and random forest was compared. The results demonstrated that the random forest model exhibited higher prediction accuracy and generalization performance, which was further validated by random data set extraction. Additionally, the effect of the partition ratio of the data set on the evaporation rate was studied using three partitions (10%, 20%, and 30%) as test sets to compare model performance. The results indicated that the model performance is better when the test set is 20% and all the constructed model converge. Furthermore, the mean absolute error (MAE) and mean squared error (MSE) were used to evaluate model performance. The study then established the evaporation rate prediction model and explored the relationship between the height-radius ratio and optimized evaporation rate through an enumeration method. By calculating the characteristic importance of the four parameters (height, diameter, height-radius ratio, and evaporation efficiency), a ratio of 6 was found to achieve the optimal evaporation rate. Finally, the optimization of the evaporator structural size could increase the evaporation rate and promote the application of interfacial evaporation in solar desalination.

ACKNOWLEDGMENTS

This work was supported by the Basic Science Center Program for Ordered Energy Conversion of the National Natural Science Foundation of China (NNSFC) (No. 51888103), NNSFC (Nos. 51706039 and 51606192), Fundamental Research Funds for the Central Universities of China (Grant No. 2572020BF01), and the CAS Pioneer Hundred Talents Program and Beijing Nova Program (No. Z211100002121087).

AUTHOR DECLARATIONS

Conflict of Interest

The authors have no conflicts to disclose.

Author Contributions

D.Q. and M.Y. contributed equally to this work.

Degao Qiao: Data curation (equal); Investigation (equal); Methodology (equal); Software (equal); Visualization (equal); Writing – original draft (equal). **Ming Yang:** Conceptualization (equal); Funding acquisition (equal); Resources (equal); Supervision (equal); Validation (equal); Visualization (equal); Writing – original draft (equal); Writing – review & editing (equal). **Yin Gao:** Supervision (equal); Validation (equal); Visualization (equal). **Jue Hou:** Validation (equal); Writing – review & editing (equal). **Xingli Zhang:** Funding acquisition (equal); Investigation (equal); Supervision (equal); Validation (equal); Visualization (equal). **Hang Zhang:** Conceptualization (equal); Funding acquisition (equal); Investigation (equal); Project administration (equal); Supervision (equal); Validation (equal); Visualization (equal).

DATA AVAILABILITY

The data that support the findings of this study are available within the article.

REFERENCES

- ¹M. Gao, C. K. Peh, F. L. Meng, and G. W. Ho, "Photothermal membrane distillation toward solar water production," *Small Methods* **5**, 2001200 (2021).
- ²L. Zang, C. Finnerty, S. Zheng, K. Conway, L. Sun, J. Ma, and B. Mi, "Interfacial solar vapor generation for desalination and brine treatment: Evaluating current strategies of solving scaling," *Water Res.* **198**, 117135 (2021).
- ³Y. Qiu, M. Lee, J. Chen, and Q. Zhang, "Effect of light intensity on solar-driven interfacial steam generation," *Nanoscale* **13**, 20387–20395 (2021).
- ⁴Z. Li, X. Xu, X. Sheng, P. Lin, J. Tang, L. Pan, Y. V. Kaneti, T. Yang, and Y. Yamauchi, "Solar-powered sustainable water production: State-of-the-art technologies for sunlight-energy-water nexus," *ACS Nano* **15**, 12535–12566 (2021).
- ⁵J. Liang, H. Liu, J. Yu, L. Zhou, and J. Zhu, "Plasmon-enhanced solar vapor generation," *Nanophotonics* **8**, 771–786 (2019).
- ⁶N. Xu, J. Li, C. Finnerty, Y. Song, L. Zhou, B. Zhu, P. Wang, B. Mi, and J. Zhu, "Going beyond efficiency for solar evaporation," *Nat. Water* **1**, 494 (2023).
- ⁷S. Liu, S. Li, and M. Lin, "Understanding interfacial properties for enhanced solar evaporation devices: From geometrical to physical interfaces," *ACS Energy Lett.* **8**(4), 1680–1687 (2023).
- ⁸Y. Yang, J. Han, H. Zhai, J. Chen, Q. Jiang, S. Chen, B. Li, and X. Cao, "Prediction and screening of glass properties based on high-throughput molecular dynamics simulations and machine learning," *J. Non-Cryst. Solids* **597**, 121927 (2022).
- ⁹S. K. Joshi, S. K. Singh, and S. Dubey, "Machine learning and molecular dynamics based models to predict the temperature dependent elastic properties of silver nanowires," *Int. J. Comput. Methods Eng. Sci. Mech.* **24**, 345–353 (2023).
- ¹⁰Y. Wang, A. W. Kandeal, A. Swidan, S. W. Sharshir, G. B. Abdelaziz, M. A. Halim, A. E. Kabeel, and N. Yang, "Prediction of tubular solar still performance by machine learning integrated with Bayesian optimization algorithm," *Appl. Therm. Eng.* **184**, 116233 (2021).
- ¹¹X. Liu, F. Chen, Y. Li, H. Jiang, D. D. Mishra, F. Yu, Z. Chen, C. Hu, Y. Chen, L. Qu, and W. Zheng, "3D hydrogel evaporator with vertical radiant vessels breaking the trade-off between thermal localization and salt resistance for solar desalination of high-salinity," *Adv. Mater.* **34**(36), 2203137 (2022).
- ¹²Y. Liu, B. Luo, H. Liu, M. He, R. Wang, L. Wang, Z. Quan, J. Yu, and X. Qin, "3D printed electrospun nanofiber-based pyramid-shaped solar vapor generator with hierarchical porous structure for efficient desalination," *Chem. Eng. J.* **452**, 139402 (2023).
- ¹³X. Zheng, Y. Bao, A. Huang, G. Qin, and M. He, "3D printing double-layer hydrogel evaporator with surface structures for efficient solar steam generation," *Sep. Purif. Technol.* **306**, 122741 (2023).
- ¹⁴L. Zhou, Y. Tan, J. Wang, W. Xu, Y. Yuan, W. Cai, S. Zhu, and J. Zhu, "3D self-assembly of aluminium nanoparticles for plasmon-enhanced solar desalination," *Nat. Photonics* **10**(6), 393–398 (2016).
- ¹⁵H. W. Lim, S. H. Park, and S. J. Lee, "3D thermoresponsive hydrogel with enhanced water uptake and active evaporation for effective interfacial solar steam generation," *Desalination* **550**, 116368 (2023).
- ¹⁶Z. Jin, M. Zhang, H. Mei, H. Liu, L. Pan, Y. Yan, L. Cheng, and L. Zhang, "3D-printed chiral torsion Janus evaporator with enhanced light utilization towards ultrafast and stable solar-water desalination," *Carbon* **202**, 159–168 (2023).
- ¹⁷Y. Chen, J. Yang, J. Guo, and F. Fang, "A 3D photothermal bar for efficient steam generation," *J. Environ. Chem. Eng.* **11**(1), 109179 (2023).
- ¹⁸Y. Cai, Y. Dong, K. Wang, D. Tian, J. Qu, J. Hu, J. Lee, J. Li, and K.-H. Kim, "A polydimethylsiloxane-based sponge for water purification and interfacial solar steam generation," *J. Colloid Interface Sci.* **629**, 895–907 (2023).
- ¹⁹X. Li, S. Tanyan, S. Xie, R. Chen, Q. Liao, X. Zhu, and X. He, "A 3D porous PDMS sponge embedded with carbon nanoparticles for solar driven interfacial evaporation," *Sep. Purif. Technol.* **292**, 120985 (2022).
- ²⁰M. Cong, F. Wang, Y. Zhang, L. Xie, Y. Lei, K. Sun, and L. Dong, "An array structure of polydopamine/wood solar interfacial evaporator for high-efficiency water generation and desalination," *Sol. Energy Mater. Sol. Cells* **249**, 112052 (2023).
- ²¹H. Lim and S. K. Kim, "An easily scalable, durable, and highly efficient three-dimensional solar evaporator inspired by a rice paddy field," *Desalination* **548**, 116251 (2023).
- ²²H. Duan, M. Wang, Z. Zhang, J. Zhen, and W. Lv, "Biomass-derived photothermal carbon aerogel for efficient solar-driven seawater desalination," *J. Environ. Chem. Eng.* **11**(2), 109295 (2023).
- ²³Z. Qin, H. Sun, Y. Tang, S. Yin, L. Yang, M. Xu, and Z. Liu, "Bioinspired hydrophilic-hydrophobic Janus composites for highly efficient solar steam generation," *ACS Appl. Mater. Interfaces* **13**(16), 19467–19475 (2021).
- ²⁴Z. Zhang, Z. Feng, H. Qi, Y. Chen, Y. Chen, Q. Deng, and S. Wang, "Carbonized sorghum straw derived 3D cup-shaped evaporator with enhanced evaporation rate and energy efficiency," *Sustain. Mater. Technol.* **32**, e00414 (2022).
- ²⁵H. Ma, S. Zhang, X. Guo, M. Liu, S. Wu, J. Tang, and C. Bao, "Cone/plate structured photothermal evaporator with obviously improved evaporation properties by suppressing thermal conduction-caused heat loss," *Sep. Purif. Technol.* **307**, 122754 (2023).
- ²⁶K. Sun, H. Cui, R. Xu, L. Wang, M. Li, Z. Yang, M. Zhao, and N. Wei, "Constructing of 3D porous composite materials of NiAl/CNTs for highly efficient solar steam generation," *Sol. Energy Mater. Sol. Cells* **240**, 111722 (2022).
- ²⁷R. Xu, H. Cui, K. Sun, X. Song, K. Yang, N. Wei, C. Hou, and M. Zhao, "Controllable 3D interconnected featured pore structure of transition metal borides-carbonitride/MoS₂ for efficiently solar evaporation and wastewater purification," *Chem. Eng. J.* **446**, 137275 (2022).
- ²⁸H. M. Wilson, S. Raheman, A. R. H. W. Lim, and S. J. Lee, "Conversion of hazardous diesel soot particles into a novel highly efficient 3D hydrogel for solar desalination and wastewater purification," *ACS Omega* **8**(2), 2740–2751 (2023).
- ²⁹L. Chen, J. Ren, J. Gong, J. Qu, and R. Niu, "Cost-effective, scalable fabrication of self-floating xerogel foam for simultaneous photothermal water evaporation and thermoelectric power generation," *Chem. Eng. J.* **454**, 140383 (2023).
- ³⁰L. Qiao, N. Li, L. Luo, J. He, Y. Lin, J. Li, L. Yu, C. Guo, P. Murto, and X. Xu, "Design of monolithic closed-cell polymer foams via controlled gas-foaming for high-performance solar-driven interfacial evaporation," *J. Mater. Chem. A* **9**(15), 9692–9705 (2021).
- ³¹C. Dang, X. Zhang, L. Huang, G. Xu, L. Gu, X. Cao, and M. Zhu, "Design of solar evaporator with well-aligned and multi-scale fluid channels based on convection tuning for stable and efficient brine desalination," *Desalination* **550**, 116408 (2023).
- ³²Z. Hu, L. Ren, Q. Zhang, and X. Xiao, "Designing Janus ZrC@fabric-based evaporator through weaving craft for stable solar interfacial desalination," *Mater. Lett.* **333**, 133619 (2023).
- ³³N. Hu, Y. Xu, Z. Liu, M. Liu, X. Shao, and J. Wang, "Double-layer cellulose hydrogel solar steam generation for high-efficiency desalination," *Carbohydr. Polym.* **243**, 116480 (2020).
- ³⁴D. Xu, H. Zhong, M. G. Li, S. S. To, and L. Lu, "Efficient plasmonic enhanced solar evaporation achieved by laser-assisted Cu/graphene nanocomposite," *Carbon* **204**, 231–237 (2023).
- ³⁵Z. Wang, J. Gao, J. Zhou, J. Gong, L. Shang, H. Ye, F. He, S. Peng, Z. Lin, Y. Li, and F. Caruso, "Engineering metal-phenolic networks for solar desalination with directional salt crystallization," *Adv. Mater.* **35**(1), 2209015 (2023).
- ³⁶X. Li, J. Li, J. Lu, N. Xu, C. Chen, X. Min, B. Zhu, H. Li, L. Zhou, S. Zhu, T. Zhang, and J. Zhu, "Enhancement of interfacial solar vapor generation by environmental energy," *Joule* **2**(7), 1331–1338 (2018).
- ³⁷L. Qiao, S. Li, N. Li, S. Wang, C. Wang, X. Meng, P. Murto, and X. Xu, "Fabrication of monophile polymer foams via rotating gas foaming: Hybrid applications in solar-powered interfacial evaporation and water remediation," *Solar RRL* **6**(8), 2200241 (2022).

- ³⁸J. Zhu, J. Liu, J. Liu, S. Guo, S. Lu, Y. Lv, and B. Song, "FDM 3D-printed volcanic-shaped structure for ultrafast solar-driven interfacial evaporation and efficient energy utilization," *Desalination* **548**, 116275 (2023).
- ³⁹L. Ai, Y. Xu, S. Qin, Y. Luo, W. Wei, X. Wang, and J. Jiang, "Facile fabrication of Ni₅P₄-NiMoO_x nanorod arrays with synergistic thermal management for efficient interfacial solar steam generation and water purification," *J. Colloid Interface Sci.* **634**, 22–31 (2023).
- ⁴⁰Z. Yuan, "Flexible and robust nanofiber sponge with superior capacity to transport water for efficient and sustained solar-driven interfacial evaporation," *Desalination* **550**, 116399 (2023).
- ⁴¹A. Caratenuto, A. Aljwirah, Y. Tian, X. Liu, Y. Wan, and Y. Zheng, "Forest waste to clean water: Natural leaf-guar-derived solar desalinator," *Nanoscale* **13**(42), 17754–17764 (2021).
- ⁴²D. P. Storer, J. L. Phelps, X. Wu, G. Owens, N. I. Khan, and H. Xu, "Graphene and rice-straw-fiber-based 3D photothermal aerogels for highly efficient solar evaporation," *ACS Appl. Mater. Interfaces* **12**(13), 15279–15287 (2020).
- ⁴³Z. Xu, X. Ran, D. Wang, M. Zhong, and Z. Zhang, "High efficient 3D solar interfacial evaporator: Achieved by the synergy of simple material and structure," *Desalination* **525**, 115495 (2022).
- ⁴⁴F. Zhao, X. Zhou, Y. Shi, X. Qian, M. Alexander, X. Zhao, S. Mendez, R. Yang, L. Qu, and G. Yu, "Highly efficient solar vapour generation via hierarchically nanostructured gels," *Nat. Nanotechnol.* **13**(6), 489–495 (2018).
- ⁴⁵K. Lan, Y. Deng, A. Huang, S.-Q. Li, G. Liu, and H.-L. Xie, "Highly-performance polyimide as an efficient photothermal material for solar-driven water evaporation," *Polymer* **256**, 125177 (2022).
- ⁴⁶C. Shi, X. Zhang, A. Nilghaz, Z. Wu, T. Wang, B. Zhu, G. Tang, B. Su, and J. Tian, "Large-scale production of spent coffee ground-based photothermal materials for high-efficiency solar-driven interfacial evaporation," *Chem. Eng. J.* **455**, 140361 (2023).
- ⁴⁷Z. Yang, D. Yang, C. Yang, K. Yu, X. Chen, F. Qu, and W. Guo, "Magnetically recyclable 3D water evaporator for desalination and purification of oil-contaminated seawater," *Desalination* **546**, 116187 (2023).
- ⁴⁸Y. Chen, J. Yang, L. Zhu, S. Wang, X. Jia, Y. Li, D. Shao, L. Feng, and H. Song, "Marangoni-driven biomimetic salt secretion evaporator," *Desalination* **548**, 116287 (2023).
- ⁴⁹L. Chen, Y. Wu, W. Xing, Q. Su, L. Tang, H. Xue, and J. Gao, "Mechanically robust composite hydrogels for high performance solar driven interface evaporation," *Chem. Eng. Sci.* **267**, 118330 (2023).
- ⁵⁰T. Gao, Y. Wang, X. Wu, P. Wu, X. Yang, Q. Li, Z. Zhang, D. Zhang, G. Owens, and H. Xu, "More from less: Improving solar steam generation by selectively removing a portion of evaporation surface," *Sci. Bull.* **67**(15), 1572–1580 (2022).
- ⁵¹X. Zhang, D. Qiao, and M. Yang, "Structural effects of graphene interface on the performance of solar-driven water evaporation," *Mol. Phys.* e2283141 (published online) (2023).
- ⁵²F. Liu, D. Lou, E. Liang, Y. Gu, Z. Wang, X. Shi, R. Bradley, B. Zhao, and W. Wu, "Nanosecond laser patterned porous graphene from monolithic mesoporous carbon for high-performance solar thermal interfacial evaporation," *Adv. Mater. Technol.* **6**(12), 2101052 (2021).
- ⁵³H. M. Wilson, Tushar, S. Raheman Ar, and N. Jha, "Plant-derived carbon nanospheres for high efficiency solar-driven steam generation and seawater desalination at low solar intensities," *Sol. Energy Mater. Sol. Cells* **210**, 110489 (2020).
- ⁵⁴M. Y. Wong, Y. Zhu, T. C. Ho, A. Pan, and C. Y. Tso, "Polypyrrole-reduced graphene oxide coated delignified wood for highly efficient solar interfacial steam generation," *Appl. Therm. Eng.* **219**, 119686 (2023).
- ⁵⁵Z. Chen, Q. Li, and X. Chen, "Porous graphene/polyimide membrane with a three-dimensional architecture for rapid and efficient solar desalination via interfacial evaporation," *ACS Sustain. Chem. Eng.* **8**(36), 13850–13858 (2020).
- ⁵⁶C. Yu and Z. Dai, "Characterizing the wetting behavior of 2D materials: a review," *J. Mater. Inf.* **3**, 20 (2023).
- ⁵⁷Y. Wang, X. Wu, X. Yang, G. Owens, and H. Xu, "Reversing heat conduction loss: Extracting energy from bulk water to enhance solar steam generation," *Nano Energy* **78**, 105269 (2020).
- ⁵⁸X. Gu, K. Dong, L. Peng, L. Bian, Q. Sun, W. Luo, and B. Zhang, "Round-the-clock interfacial solar vapor generator enabled by form-stable phase change materials with enhanced photothermal conversion capacity," *Energy Convers. Manage.* **277**, 116634 (2023).
- ⁵⁹C. Tian, J. Liu, R. Ruan, X. Tian, X. Lai, L. Xing, Y. Su, W. Huang, Y. Cao, and J. Tu, "Sandwich photothermal membrane with confined hierarchical carbon cells enabling high-efficiency solar steam generation," *Small* **16**(23), 2000573 (2020).
- ⁶⁰Y. Li, W. Hong, H. Li, Z. Yan, S. Wang, X. Liu, B. Li, H. Jiang, and X. Niu, "Solar absorber with tunable porosity to control the water supply velocity to accelerate water evaporation," *Desalination* **511**, 115113 (2021).
- ⁶¹P. Wang, Q. Cui, Q. Zeng, Q. Jiang, and Q. Ren, "Solar interfacial evaporation based oil/water separation from emulsion using a wood-melamine/calcium alginate composite structure," *Solar Energy* **250**, 59–69 (2023).
- ⁶²L. Wang, Y. Feng, Q. Liu, and G. Liu, "Solar-thermo-radiative evaporator for continuous steam generation and salt harvesting," *Solar Energy* **250**, 347–354 (2023).
- ⁶³B. Shao, Y. Wang, X. Wu, Y. Lu, X. Yang, G. Y. Chen, G. Owens, and H. Xu, "Stackable nickel-cobalt@polydopamine nanosheet based photothermal sponges for highly efficient solar steam generation," *J. Mater. Chem. A* **8**(23), 11665–11673 (2020).
- ⁶⁴F. Gong, W. Wang, H. Li, D. (David) Xia, Q. Dai, X. Wu, M. Wang, J. Li, D. V. Papavassiliou, and R. Xiao, "Solid waste and graphite derived solar steam generator for highly-efficient and cost-effective water purification," *Appl. Energy* **261**, 114410 (2020).
- ⁶⁵P. Zhang, J. Li, L. Lv, Y. Zhao, and L. Qu, "Vertically aligned graphene sheets membrane for highly efficient solar thermal generation of clean water," *ACS Nano* **11**(5), 5087–5093 (2017).
- ⁶⁶B. Zhu, J. Zhao, Y. Meng, Z. Liu, N. Yu, L. Zhang, and Z. Chen, "Watermelon flesh-derived carbon aerogel with hierarchical porous structure for interfacial solar steam generation," *Solar RRL* **6**(8), 2200270 (2022).
- ⁶⁷M. Yang, X. Zhang, and H. Zhang, "Effects of monovacancy on thermal properties of bilayer graphene nanoribbons by molecular dynamics simulations," *J. Therm. Sci.* **30**(6), 1917–1924 (2021).
- ⁶⁸S. Chen, M. Yang, B. Liu, M. Xu, T. Zhang, B. Zhuang, D. Ding, X. Huai, and H. Zhang, "Enhanced thermal conductance at the graphene-water interface based on functionalized alkane chains," *RSC Adv.* **9**(8), 4563–4570 (2019).